JATIS Journal of Astronomical Telescopes, Instruments, and Systems

RESEARCH PAPER

# Simulating the effect of chromatic beam wander on the ELT/METIS high-contrast imaging performance

**André Boné**[a,*] **Christian Delacroix**[b] **and Olivier Absil**[b]
[a]Max-Planck-Institut für Astronomie, Heidelberg, Germany
[b]Université de Liège, STAR Institute, Liège, Belgium

**ABSTRACT.** Mid-infrared European Extremely Large Telescope (ELT) Imager and Spectrograph (METIS), one of the first-generation instruments of the upcoming ELT, is designed toward the direct detection of exoplanets, using high-contrast imaging (HCI) techniques. However, it is well known that noncommon path aberrations (NCPA) limit HCI performance. In particular, quasi-static NCPA creates speckles that evolve on the same time scale as angular differential imaging (ADI) sequences, which are typically used to estimate and subtract the stellar speckle field. It is therefore crucial to model NCPA correctly during the instrument design phase to derive requirements on wavefront control algorithms that minimize their effects. We explore the chromatic beam wander caused by atmospheric refraction on METIS as a source of time-variable NCPA and its impact on HCI performance. We study the vortex coronagraph case, which is expected to set the requirements for NCPA correction. We propagate wavefronts through a model of the full METIS instrument in pupil tracking mode, taking into account the contribution of each optical element to phase aberrations in the presence of chromatic beam wander. We also model the associated amplitude aberrations that develop upon propagation. The beams are propagated within a 4-h interval, from which we extract a 1-h observing sequence close to the zenith as a representative ADI sequence. We show that the time-variable NCPA created by chromatic beam wander already reaches, and sometimes exceeds, the allocated NCPA budget within METIS, even though its effect is smaller than the effect of water vapor seeing at N-band. A closed-loop correction is needed to compensate for their effect, but even so, the HCI performance may be limited by the associated amplitude aberrations, which cannot be corrected within METIS.

 [DOI: 10.1117/1.JATIS.12.1.014001]

**Keywords:** high-contrast imaging; optical propagation; noncommon path aberrations; extremely large telescope; Mid-infrared ELT Imager and Spectrograph

Paper 25131G received Apr. 28, 2025; revised Nov. 12, 2025; accepted Dec. 18, 2025; published Jan. 12, 2026.

## 1 Introduction

The advent of giant segmented ground-based telescopes, such as the European Extremely Large Telescope (ELT[1]), is bound to revolutionize many fields of astronomy and astrophysics, among which is the direct detection of exoplanets with high-contrast imaging (HCI) techniques. The mid-infrared ELT imager and spectrograph (METIS[2]), one of the first-generation instruments of the ELT, is specifically designed toward this goal, with the ultimate objective to detect rocky

*Address all correspondence to André Boné, bone@mpia.de

planets around nearby stars.[3] To optimize the design of METIS for HCI performance, Refs. 4 and 5 performed a series of end-to-end simulations, taking into account the adaptive optics performance[6,7] and various noise sources, including telescope imperfections such as ELT-M1 phasing errors, misaligned/missing segments, nonuniform segment reflectivity, wind shake, etc., as well as instrument-specific errors, such as pupil alignment, pointing errors, noncommon path aberrations (NCPA), residual atmospheric dispersion after partial compensation, etc. These simulations highlight the crucial contribution of NCPA to the achievable HCI performance. This result is not surprising, as NCPA is understood to be one of the main limitations to the performance of current HCI instruments on 10-m class telescopes (see e.g., Ref. 8). The static part of NCPA is generally benign to the HCI performance, as its signature in terms of focal-plane speckles can be removed by post-processing techniques such as angular differential imaging (ADI[9]), where field rotation is used in pupil-stabilized mode to disentangle rotating astrophysical sources from fixed speckles. Conversely, slowly varying NCPA—also referred to as quasi-static NCPA—are a dominating factor to the sensitivity of HCI instruments to faint companions, because they create speckles that evolve on the same timescale (i.e., minutes to hours) as planetary signals in ADI sequences. Other important contributors to wavefront quality, such as such low-wind effect and wind-driven halo,[10] are also known to be major sources of performance limitations in HCI instruments, but these will not be considered in this work.

Because they are identified as a potential bottleneck to HCI performance in general, and of the METIS HCI performance in particular, NCPA are an active subject of research in the field of HCI (see e.g., Ref. 11 for a review of NCPA measurement and correction techniques). In the context of METIS, due to hardware constraints, NCPA sensing will be purely based on focal-plane images obtained with the imaging science camera (referred to as IMG). NCPA sensing and control will be divided into two parts: (i) a pointing sensing and control algorithm (QACITS[12]) dedicated to vortex coronagraphy, for which pointing errors are particularly harmful, and (ii) a higher-order wavefront sensing and control algorithm, which is planned to be based on the use of an asymmetric pupil mask.[13–15] In addition, NCPA will be carefully measured during the assembly, integration, and test (AIT) phase of the instrument, to be used as a reference for future on-sky operations.

To predict the effect of NCPA on the METIS HCI performance and to properly design the wavefront control algorithms required to mitigate their effect, it is crucial to build a realistic model for these aberrations. In our previous work,[5] we referred to two main sources of variability for NCPA—water vapor seeing and chromatic beam wander—and provided a first glimpse of how they are expected to affect the METIS HCI performance. In Ref. 16, we described in more detail the effect of water vapor seeing, a chromatic component of atmospheric turbulence that is particularly harmful for HCI operations in the mid-infrared at ELT scale. Here, we describe and analyze for the first time the other major source of slowly variable NCPA in METIS: chromatic beam wander. This source is related to the variations in the optical propagation of slightly offset beams through the METIS optical train at different wavelengths, due to differential atmospheric refraction. The present study aims to quantify this effect and its consequences on the METIS HCI performance. The rest of the paper is structured as follows. In Sec. 2 (Methodology), we explain how we propagate the wavefront through the atmosphere model, the ELT, and METIS. Sec. 3 (Results) presents the wavefront phase and amplitude errors obtained after propagation and discusses the ADI performance using these results. Finally, Sec. 5 concludes this work and presents some perspectives for extension to other ELT instruments.

## 2 Methodology

The METIS HCI modes rely on two main coronagraphic concepts: the vortex coronagraph and the apodizing phase plate.[17,18] For the present study, we follow Ref. 4 and focus on the L-band, ring-apodized implementation of the vortex coronagraph, which is expected to provide the deepest contrasts among the METIS HCI modes and also to be the most sensitive to aberrations. This coronagraphic mode is therefore expected to set the requirements on NCPA amplitude and correction accuracy. We also discuss the case of the N-band vortex coronagraph, where it is interesting to compare the effect of chromatic beam wander to the strong effect of water vapor seeing.

To assess the effect of NCPA on HCI performance, we use the framework described in Ref. 4, which consists of propagating aberrated wavefronts through a model of the (ring-apodized) vortex coronagraph. Here, we take into account both phase and amplitude aberrations, and their variation over time, as a target star is tracked across the sky. To provide an easy comparison with the results presented by Ref. 4, we produce a 4-h NCPA simulation, from which we extract a 1-h observing sequence in pupil-tracking mode around the meridian, for a star with a declination of −16 deg, which culminates at an altitude of 81 deg at Cerro Armazones. Because of the small zenith angle, these observations do not require the use of an atmospheric dispersion corrector (ADC) and are representative of a typical HCI observing sequence in terms of chromatic beam wander. Here, it must be noted that METIS features two static atmospheric dispersion compensators (ADC), both made up of two prisms, optimized respectively for zenith distances of 25° and 41°. These static ADC never provide a perfect correction and are, instead, designed to assure that the effect of atmospheric dispersion at various elevations does not become larger than for the no-ADC situation at zenith angles between about 10° and 15° and that the effect of dispersion on PSF elongation remains negligible in our HCI error budget.[4] These are precisely the angles explored within the considered ADI sequence in this work, which makes our work applicable to any other zenith distance up to about 50°, without the extra burden of having to include an ADC in our optical path. Although differential refraction is smaller at low airmasses, the amount of field rotation and the variation in altitude across the sequence are larger than at high airmasses, which maximizes the temporal variations of NCPAs due to chromatic beam wander. A classical angular differential imaging (cADI) algorithm[9] is then applied to the simulated time sequence of coronagraphic images to assess the sensitivity of METIS to faint off-axis companions through contrast curves, which are computed as in Ref. 19.

In the following sections, we will propagate beams from the sky up to the relevant METIS pupil planes where adaptive optics wavefront sensing and coronagraphy are implemented. This corresponds respectively to the pupil plane referred to as SCA-PP2 within the single-conjugate adaptive optics (SCAO) path, which is a good proxy for the focal plane SCA-FP2 where the pyramid wavefront sensor is placed, and to the pupil plane PP1 in IMG-LM and IMG-N (imager paths at LM and N bands, respectively), where the Lyot stops of the vortex coronagraphs are located. At these planes, we evaluate the phase and amplitude aberrations. An overview of these optical paths can be seen in Fig. 1.

We consider the central field for an object placed at infinity. This object produces three beams with different wavelengths: 2.1 $\mu$m for the SCAO path, 3.8 $\mu$m for the IMG LM band path, and 11 $\mu$m for the IMG N band path. The beams are propagated through the atmosphere, the ELT telescope, and the METIS optical system up to the SCAO or the IMG pupils.

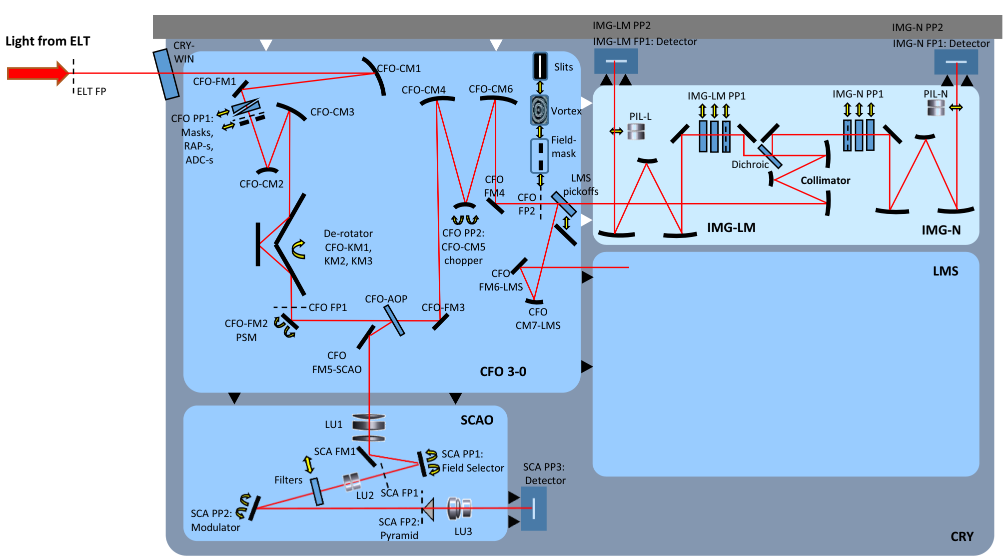


**Fig. 1** Optical diagram overview of METIS.[2]

### 2.1 METIS Optical Design Description

The ELT re-images incoming beams at the ELT-FP, just before the cryostat window. This is done through six mirrors: three powered mirrors (ELT-M1-3), one deformable mirror for adaptive optics (ELT-M4), one flat steering mirror for alignment (ELT-M5), and one folding mirror that selects the optical instrument (ELT-M6). Once inside the METIS cryostat, the light is propagated through the common fore optics (CFO) to the SCAO and IMG modules.

The CFO is a double re-imager (both Offner relays) that provides the optical interfaces between the telescope and the different METIS scientific modules (and SCAO). It is also responsible for image de-rotation, chopping, pupil stabilization, and thermal background and stray light reduction.[20,21] In this work, however, only the image de-rotation functionality is relevant. The light passes through the cryostat window into the first re-imager, which has a folding mirror (CFO-FM1) right after the first curved mirror (CFO-CM1) and before the pupil (CFO-PP1). The atmospheric dispersion compensators (ADCs) should be placed around here but, as explained above, are not considered in this work. The ring apodizer mask is also placed here, but considering that its impact on the NCPA is not significant, it is not considered for the beam propagation. The de-rotator consists of three mirrors (CFO-KM1-3), which are placed before the exit focal plane of the first relay (CFO-FP1). A fold mirror, used for pupil stabilization, directs the light to a dichroic (CFO-AOP), which reflects the wavelengths below 2.8 $\mu$m to the SCAO module and transmits the remaining wavelengths forward on the CFO. This is the end of the common path. The remaining beams are then reflected by another folding mirror toward the mirrors of the second relay (CFO-CM4-6). The intermediate mirror of this relay (CFO-CM5) is at the pupil plane, and it works as a chopper. This functionality is not relevant to this work either, even though the mandatory 1-Hz chopping pattern at N band is known to introduce a static NCPA error between the two chopped positions, which will be calibrated during AIT and precompensated accordingly in real time with the ELT-M4 deformable mirror (chopping will not be performed at LM bands). Another folding mirror (CFO-FM4) is located just before the exit focal plane of the second relay (CFO-FP2). Here, we have a wheel mechanism that provides coronagraphic elements for the science beams (not considered for the beam propagation, because their impact on the NCPA is not significant).[4] Just downstream of CFO-FP2, a pick-off mirror can be inserted into the beam to redirect the light towards another scientific module (the LM-band integral field spectrograph), but in our case, it is not placed in the beam.

After this, the light enters the IMG module, which consists of a series of three three mirror anastigmat (TMA): one in the LMN common path, one for the LM-band arm, and another for the N-band arm. The first TMA collimates the beam, which is then relayed to a dichroic that reflects the light towards the N arm and transmits it towards the LM arm. Once the majority of the starlight has been blocked by the Lyot stop, additional aberrations do not significantly affect the coronagraphic performance. They just slightly reduce the Strehl ratio on a potential planet, which we do not take into account here as the IMG is diffraction limited. Therefore, the elements downstream of the IMG pupil plane are not considered in our NCPA analysis.

The SCAO is mostly a refractive system, and its path has only four reflective surfaces, which are unpowered folding mirrors. Up to the SCA-PP2, there are six other refractive elements (five lenses and one filter).

Overall, there are 11 optical surfaces in the common path (including two surfaces for the cryostat window but excluding all ELT surfaces), 16 other surfaces on the SCAO path (refractive elements have two surfaces), 12 for the IMG-LM path, and 11 for the IMG-N path.

### 2.2 Atmosphere Layer

We model the chromatic refraction caused by the atmosphere through ZEMAX®. This raytracing software models the atmospheric refraction by applying a chromatic tilt to an incoming beam. This refraction is calculated according to Seidelmann[22] and Sinclair.[23] This model considers the altitude of the telescope above sea level (3046 m), its latitude (24.5893° S), a mean temperature of 7.5°C, a mean atmospheric pressure of 712 mbar, and a relative humidity of 22%.[24] On a 4 h observing sequence, we change the altitude angle from 60.6° (hour angle $h = -2$ h) to 81.3° ($h = 0$ h), and back to 60.6° ($h = +2$ h), and adjust the de-rotator accordingly. From here, we can extract 1-h sequences centered around different hour angles for the end-to-end

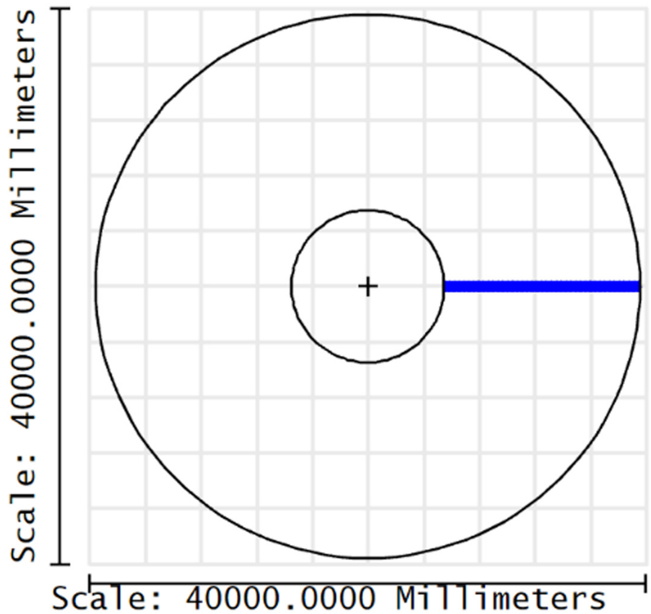


**Fig. 2** Asymmetric pupil mask (in blue) used to determine the clocking of the footprints on the optical surfaces.

simulations. We note, however, that sequences at hour angles centered around ±1h30 should be quite pessimistic in terms of HCI performance degradation, owing to the associated zenith angles (ranging from 29.4° to 15.6° in that case), and the absence of ADC in our simulations.

To explore the effect of atmospheric refraction on NCPAs, we analyze the chief ray of each beam (K, L, and N band), for each observation time, and check where it hits each optical surface, thus defining the beam's central position. We then use the marginal rays to determine the size of the beam footprint on the surfaces. The footprint is then converted to a circular shape, with the radius given by the average of the distance to the center of the marginal rays. This does not change over the simulation, so any changes of footprint size due to atmospheric dispersion are neglected. Finally, we apply an asymmetric aperture (shown in Fig. 2) and calculate the centroid of the spot diagram on each surface to check the rotation of the beams on them. The mask is removed for the remaining propagations. We use this to calculate the fraction of overlapping footprints for the common path surfaces and the beam wander and rotation as a function of the angle and de-rotator position.

### 2.3 Propagation Methods

We use the Fourier formalism (angular spectrum and Fresnel propagation) to propagate phase and amplitude aberrations through the METIS optics. This is done with the PROPER library for Python,[25] which contains all the necessary functions. The PROPER library chooses the best propagation algorithm automatically, using the method described by Lawrence.[26] We also use the technique described by Boné,[27] which conjugates every surface to the collimated space and facilitates the propagation by ignoring surface curvatures and other low order shape terms. This is done for all the METIS surfaces, but the ELT surfaces are ignored. The reason for this is that they are far from focal planes and their impact on NCPA is limited. The ELT-M6 mirror, however, is the last mirror upstream of the instrument and the nearest to a focal plane, and might have some impact on METIS. We add this mirror to the simulations to evaluate its impact.

The beam starts at the entrance pupil as a plane wavefront with uniform amplitude and phase. The aperture is defined by the $512 \times 512$ pixels image shown in Fig. 3. These 512 pixels correspond to 39920.83 mm. Zero padding is applied to oversize the grid by a factor of 2.5 ($1280 \times 1280$ pixels), to avoid unwanted vignetting, and border reflections caused by the numerical FFT.

As the beams propagate on the optical surfaces, they gain phase aberrations due to surface figure errors (SFE). These are randomly generated using an inverse power law PSD function for

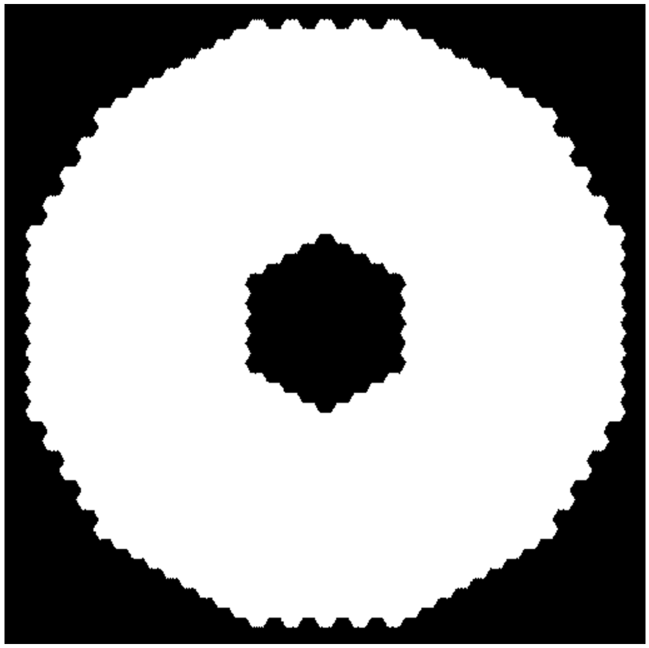

**Fig. 3** Entrance pupil aperture, corresponding to the ELT-M1.

high frequency aberrations (with slope −2), and two sets of randomized Zernike polynomials for the medium- and low-frequency aberrations (the former goes from the 21st up to the 54th term, and the latter up to the 20th term—OSA notation), as described by Boné.[27] The total power of the low-frequency Zernike terms is twice the power of the medium-frequency ones, and four times the power of the PSD function. The SFE for all surfaces is normalized to be a maximum of 15 nm RMS at any given footprint (i.e., one of the footprints will have a SFE of 15 nm RMS, whereas all the others will be lower). This is a realistic value, already used as a baseline for the METIS optical models,[21,27–29] and the surface radii are oversized to accommodate the beam wander calculated before. Figure 4 shows an example of a randomized surface. For mirrors, we apply

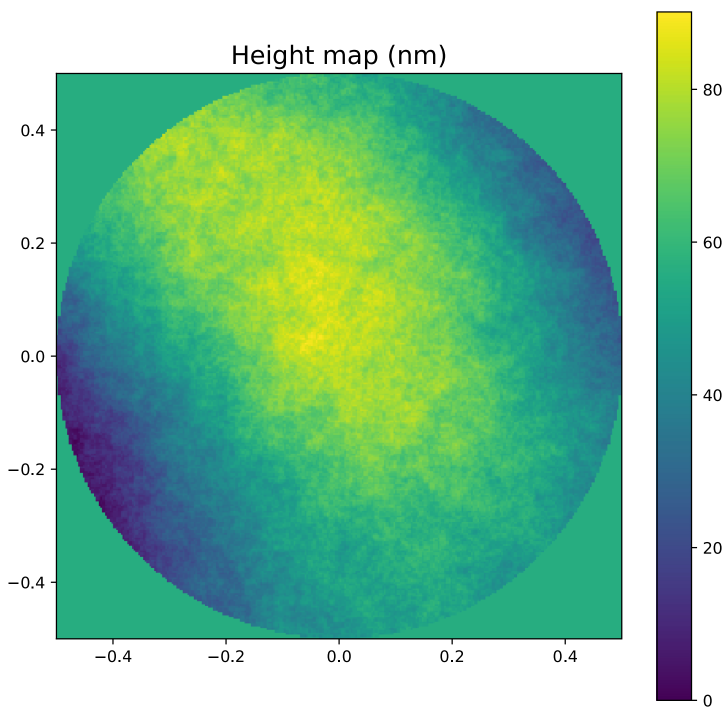


**Fig. 4** Surface figure error for one footprint (diameter normalized to 1).

**Table 1** Effects considered and excluded from the current analysis.

| Included | Excluded |
| --- | --- |
| – Atmospheric refraction | – PSF chromatic elongation |
| – Telescope pointing direction | – Chopping, nodding, telescope vibrations |
| – Beam position and orientation changes | – Beam size changes |
| – SFE for ELT-M6 | – SFE for ELT-M1 to M5, M1 phasing errors |
| – SFE for the METIS surfaces | – METIS ADC, ring apodizer, pyramid |
| – Amplitude errors due to the Talbot effect | – Amplitude errors from ELT-M1 segments |
| | – Water vapour seeing |
| | – Instabilities in METIS optics |

a multiplication factor of 2 to the surface SFE map before adding it to the phase. For refractive surfaces, however, the multiplication factor is given by $n(\lambda) - 1$, where $n(\lambda)$ is the refractive index of the material for the propagation wavelength $\lambda$.

The last surface of the common path is the front surface of a dichroic that reflects the light towards the SCAO module, or that transmits it towards the rest of the CFO. The mirror multiplication factor is applied to the SCAO path, and the refractive multiplication factor to the IMG paths, but the SFE map remains the same. In principle, we should have a similar behavior for the IMG dichroic as well, but given that the LM and N paths are analyzed with different realizations (i.e., independent simulations with different randomized surfaces), this detail is not pertinent.

As the observation proceeds, the beam rotates with respect to the surfaces up to the de-rotator and wanders due to the chromatic misalignment. We model this behavior by translating and rotating the surface maps. The optical propagation ends at the exit pupil, after the beams have travelled through all other surfaces. There, we save the amplitude and phase maps for the SCAO path and the IMG-LM or N paths. We then repeat the process for a total of 10 iterations of randomized surfaces. The various effects considered or excluded from the simulations are summarized in Table 1.

## 3 Results

### 3.1 Temporal NCPA Map Sequence

We now have 10 phase and amplitude maps for each time step at the SCAO and IMG pupils. An example of such maps is shown in Fig. 5. As expected, higher frequency phase aberrations caused by the surface sags are largely converted into amplitude errors due to the Talbot effect.[27,30] The RMS phase values change considerably from one iteration to another, with an average value of $126 \pm 34$ $\text{nm}_{\text{RMS}}$ and $117 \pm 28$ $\text{nm}_{\text{RMS}}$ for the IMG LM and N pupils, respectively, and $75 \pm 19$ $\text{nm}_{\text{RMS}}$ for the SCAO pupil. The cause for these large variations is the change in the random SFE of the optical surfaces. The variations in the footprint positions, caused by the de-rotator and atmospheric refraction, are enough to change the footprint's SFE $\sim$3 $\text{nm}_{\text{RMS}}$ from one iteration to another. This effect is then multiplied over $\sim$30 reflective surfaces, causing significant changes between iterations.

We then obtain the differential maps by subtracting the phase of the SCAO pupil from the IMG pupils and compute the associated standard deviation across the pupil (Fig. 6). As time passes, we observe that these differential phase maps maintain an almost constant wavefront error of $\approx 81 \pm 6$ $\text{nm}_{\text{RMS}}$ for the LM arm and $\approx 75 \pm 4$ $\text{nm}_{\text{RMS}}$ for the N arm. They also contain a fixed pattern corresponding to the errors introduced by the surfaces downstream of the de-rotator and a time-variable phase error pattern that corresponds to all other surfaces. The latter pattern rotates with elevation as the telescope tracks the target star, as can be seen in the video associated with Fig. 7.

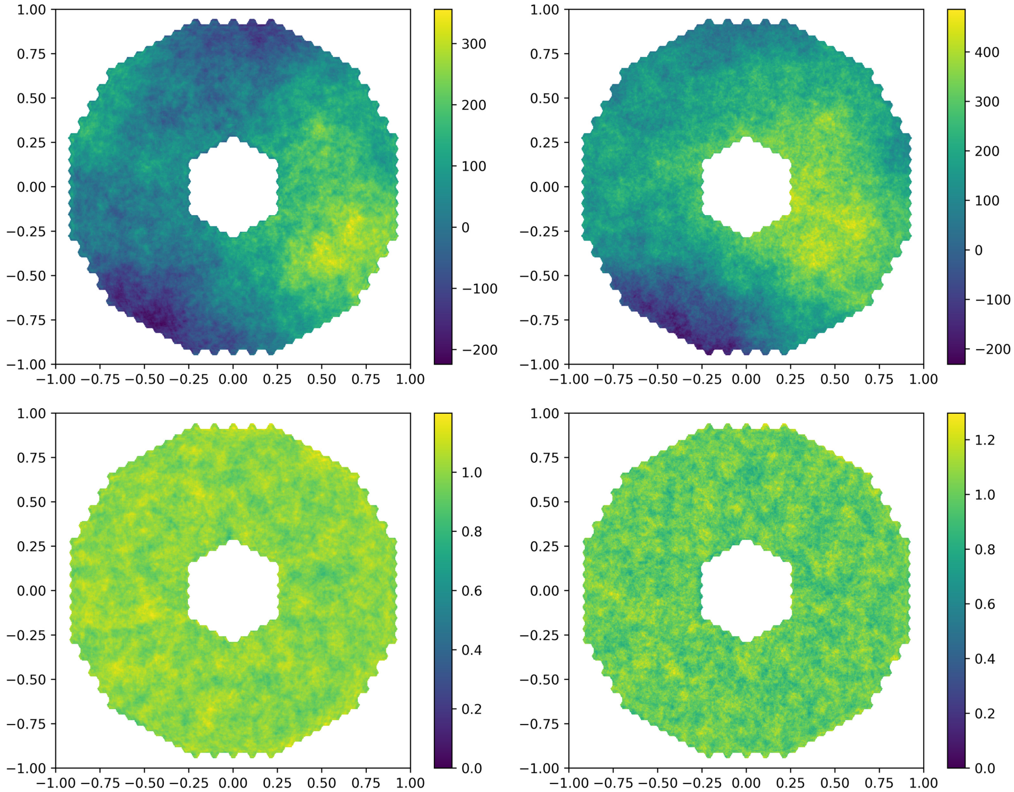

**Fig. 5** Phase (up) and amplitude (down) maps at the IMG LM pupil (on the left), and the SCAO pupil (on the right) at $t = 0$. Length units normalized to the pupil radius. Color units are in nm for phase and arbitrary units for the amplitude.

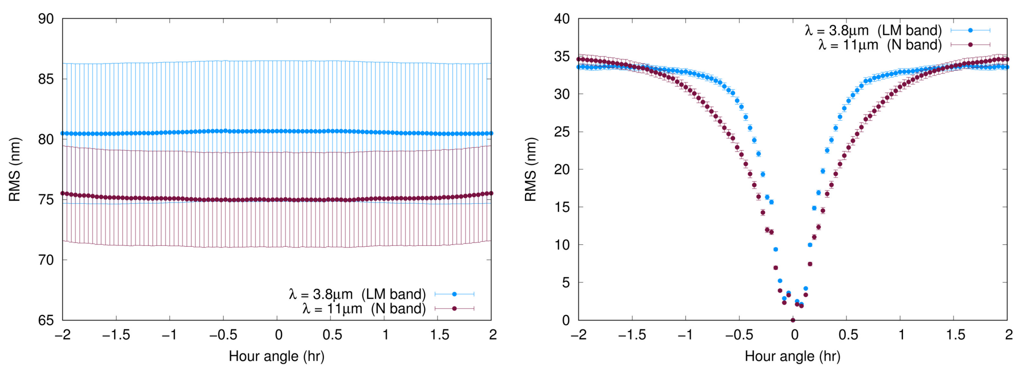


**Fig. 6** RMS differential WFE (left) and RMS dynamic WFE (right) associated with chromatic NCPA, as function of time using hr = 0 as a perfect reference. The error bars represent the standard error to the mean.

We can get rid of the fixed pattern using, e.g., the samples at $h = 0$ h as a reference and calculate the dynamic NCPA aberrations. The results are shown in Fig. 6. We see that the WFE RMS quickly increases as we get farther from the reference but remains below 35 $\text{nm}_{\text{RMS}}$ for a $\pm 2$ h observation.

### 3.2 ADI Performance in the Presence of Variable NCPA

We now integrate the differential NCPA maps into the HEEPS end-to-end simulator[4] to evaluate their impact on coronagraphic performance, both for the L-band ring-apodized vortex coronagraph (RAVC) and the N-band classical vortex coronagraph (CVC) modes of METIS. A thorough HEEPS simulation can include various sources of aberration or stellar leakage in general, such as SCAO residuals, NCPA (static, quasi-static, and dynamic), pointing drift and jitter,

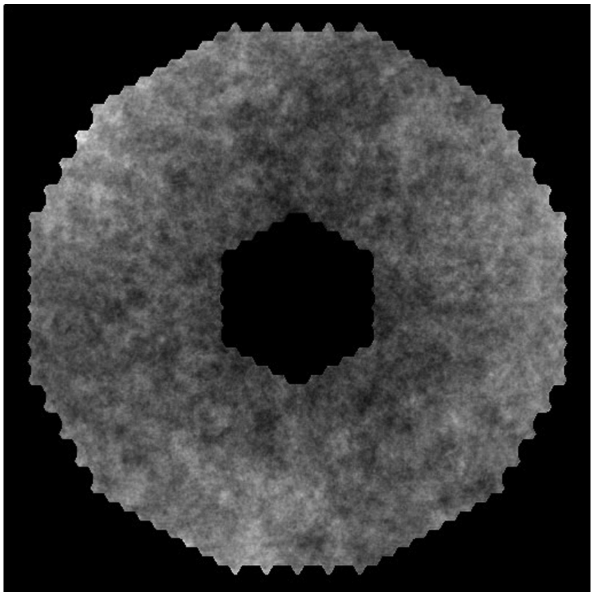

**Fig. 7** Still image extracted from a video showing the combination of a fixed phase error pattern and a rotating phase pattern (Video 1, AVI, 3.9 MB [URL: https://doi.org/10.1117/1.JATIS.12.1.014001.s1]).

water vapor seeing, pupil/apodizer drift, or phase mask chromatic leakage. In this work, however, we will only consider SCAO residuals along with NCPA maps to isolate the effect of the latter. First, we produce a METIS SCAO cube of 12,000 phase screens, equivalent to a 1-h time sequence sampled every 300 ms. This is made with the COMputing Platform for Adaptive optics SyStems (COMPASS)[31] package and features the ELT pupil with spiders (which are also added into all HEEPS simulations by default), $90 \times 90$ sub-apertures, the M4 actuator geometry, and the METIS reconstructor using a virtual DM (see Ref. 7 for details). Then, we add the NCPA maps to this cube. Because the NCPA maps are for a 4-h observing sequence of 100 frames, we first select the central 25 frames corresponding to a 1-h observation around the meridian. To match the size of the SCAO cube, we built a staircase stacking 480 of each NCPA map. Our resulting cube is then fed to HEEPS to produce 12000 coronagraphic images, subsequently processed with the cADI algorithm to obtain a contrast curve. We then repeat the process for a subset of nine iterations of randomized surfaces, chosen to be the closest to the median in terms of WFE.

In Fig. 8, we compare the resulting nine contrast curves with two other cases: (i) the SCAO-only case without any NCPA, and (ii) the SCAO + "NCPA requirements" case. The latter case includes an NCPA sequence based on a spatio-temporal decomposition, where we have used WFE values corresponding to the METIS requirements on the correction of NCPA by focal-plane wavefront sensing techniques such as QACITS[12] and the asymmetric Lyot wavefront sensor.[15] The requirement levels applied for this case are the following:

- no static NCPA at low spatial frequencies, below 10 cycles per pupil (cpp), assuming that they are perfectly corrected by closed-loop control,
- static NCPA at high spatial frequencies (>10 cpp): 35.9 $\mathrm{nm_{RMS}}$,
- quasi-static (<0.01 Hz) NCPA at low spatial frequencies (<10 cpp): 20 $\mathrm{nm_{RMS}}$,
- quasi-static (<0.01 Hz) NCPA at high spatial frequencies (>10 cpp): 20 $\mathrm{nm_{RMS}}$,
- dynamic (>0.01 Hz) NCPA at all spatial frequencies: 40 $\mathrm{nm_{RMS}}$.

In addition to investigating multiple realizations of the NCPA phase screens, we also study the influence of the hour angle on the postADI performance. When the star is not observed around meridian crossing as assumed until now, two effects are bound to affect the HCI performance: (i) the variations in the apparent rotation rate of aberrations located upstream of the derotator and (ii) the variations in angular offset between the SCAO K-band beam and the longer-wavelength science beam due to atmospheric refraction. In Fig. 9, we show that these two effects

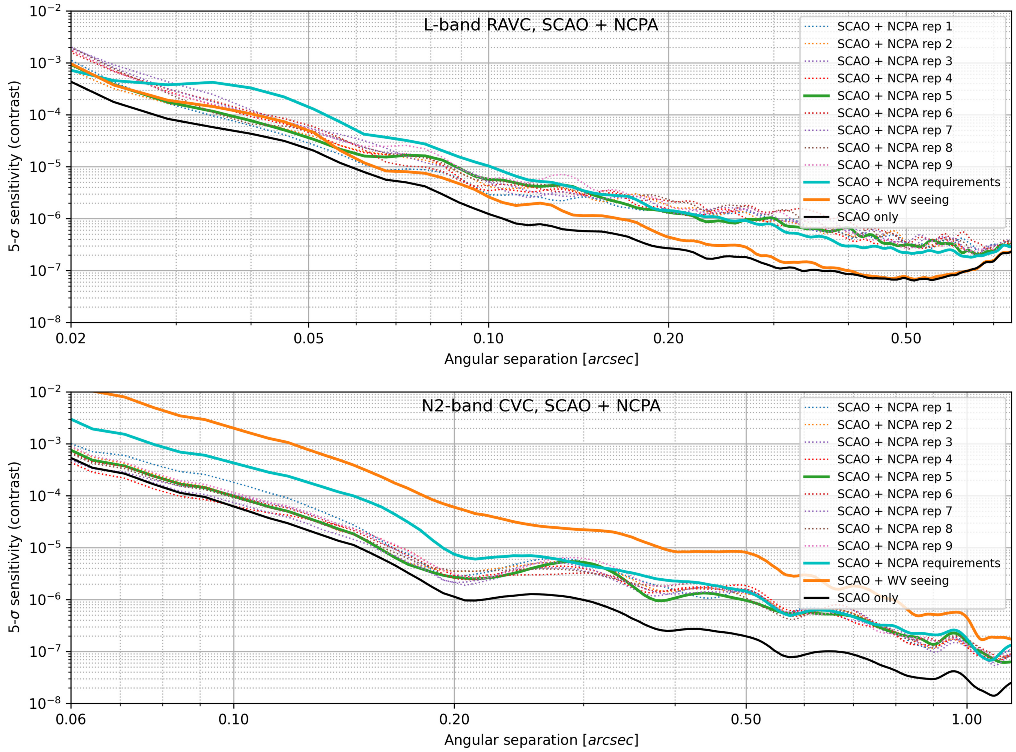


**Fig. 8** ADI contrast curves for RAVC at L band (top) and CVC at N band (bottom) over 9 repetitions of randomized NCPA surfaces. Comparison with modelized performance in accordance with METIS NCPA requirements.

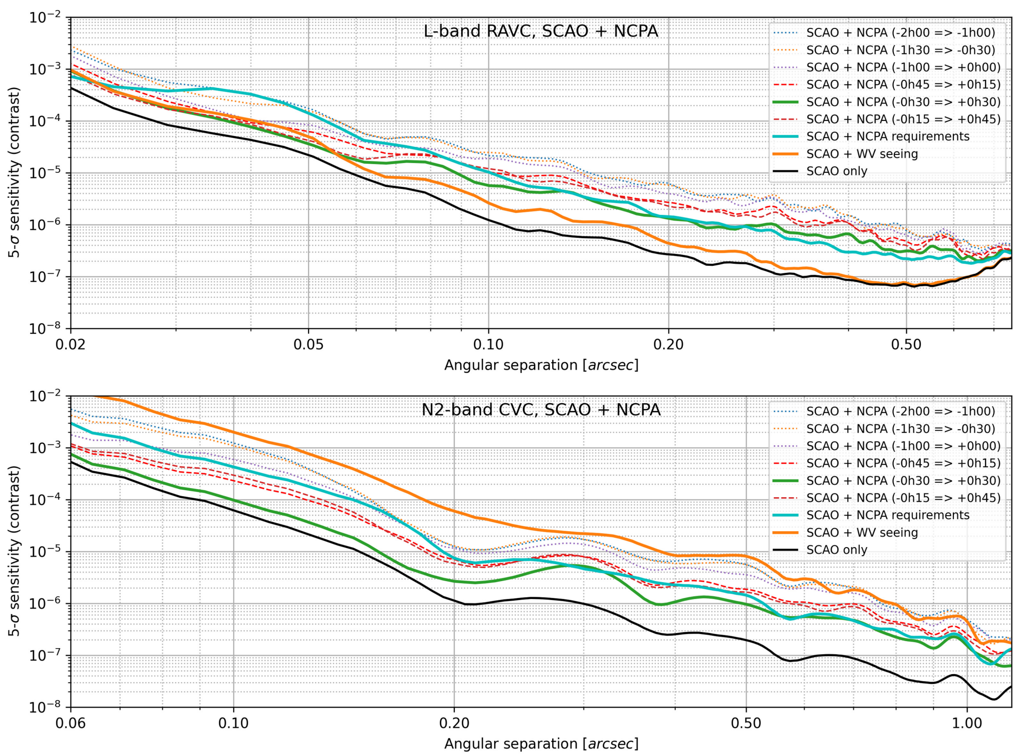


**Fig. 9** ADI contrast curves for the RAVC at L band (top) and the CVC at N band (bottom), in the presence of NCPAs due to chromatic beam wander. The center of the 1-h ADI sequence is shifted by various amounts of time compared with meridian crossing to explore the dependence of chromatic beam wander on the target trajectory in the sky.

conspire to degrade the post-ADI performance when the target star is observed far from meridian crossing, i.e., for an observing sequence not centered around a zero hour angle. These contrast curves are also influenced by the fact that field rotation is reduced when observing far from meridian crossing, which also degrades postADI performance. Compared with the situation presented in Fig. 8, the post-ADI performance can take a severe hit, by a factor up to ∼5 at the most relevant angular separations ranging from 3 to $10\,\lambda/D$, and become significantly worse than the expected ADI performance derived from the METIS internal NCPA requirements, highlighted with the cyan curve. We remind, however, that contrast curves computed farther from meridian crossing are somewhat pessimistic because of the larger zenith distance, as discussed in Sec. 2.2.

### 3.3 Influence of Variable Amplitude Errors

As described in Sec. 3.1, the chromatic beam wander effect also leads to time-variable amplitude aberrations, which also degrade the HCI performance. Here, we perform end-to-end performance simulations taking into account amplitude errors created by chromatic beam wander. As usual, SCAO residual phase screens are also taken into account in these simulations, but we do not include the effect of phase-only NCPA so that the effect of amplitude aberrations can be more readily evaluated. Figure 10 shows the postADI performance in the presence of time-variable amplitude aberrations due to chromatic beam wander for observing sequences centered around various hour angles. The rest of the simulation setup is the same as in the previous section. We compare these postADI contrast curves with the performance obtained in the presence of "median" NCPA variations around meridian crossing, illustrated by the green curve in Figs. 8 and 9. Considering an observing sequence around meridian crossing, the postADI performance in the presence of variable amplitude aberrations (brown curve in Fig. 10) is slightly better than in the presence of variable NCPA. The performance degrades when

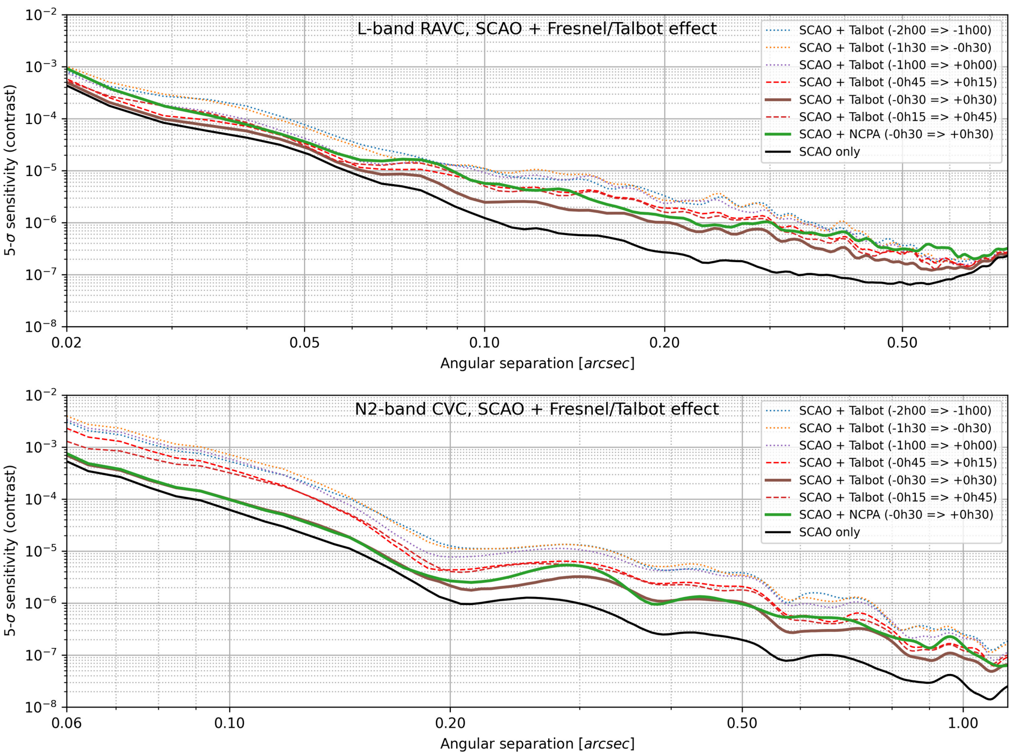


**Fig. 10** ADI contrast curves for the RAVC at L band (top) and the CVC at N band (bottom) in the presence of time-variable Talbot amplitude aberrations due to chromatic beam wander. The center of the 1-h ADI sequence is shifted by various amounts of time compared with meridian crossing to explore the dependence of chromatic beam wander on the target trajectory in the sky. These results do not include the effect of amplitude aberrations related to the ELT-M1 mirror segments, which were already studied by Ref. 5.

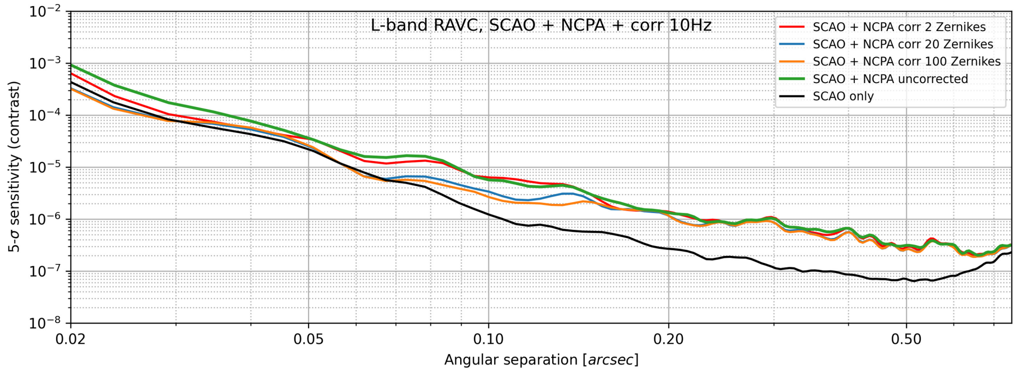


**Fig. 11** Effect of idealized closed-loop focal-plane wavefront control on the L-band METIS HCI performance in the presence of chromatic beam wander. Noiseless closed-loop correction at a loop frequency of 10 Hz is applied on various numbers of modes and compared with the uncorrected case (green) as well as to the fundamental limit set by SCAO residual phase screens (black).

observing away from the meridian crossing, as in the case of variable NCPA. This figure illustrates the need to take into account variable amplitude aberrations to produce a realistic HCI error budget.

## 4 Discussion

The present work provides a useful technique to evaluate the impact of the chromatic beam wander in the HCI modes of future astronomical instruments, such as METIS. This and other NCPA effects between the AO and science beams are limiting factors to the performance of HCI techniques, and so it is important to understand their impact on future instruments.

Our work shows that the contribution of the chromatic beam wander aberrations is considerable, matching or slightly exceeding the METIS HCI performance budget portion attributed to NCPA effects. This could potentially be fine if there were no other NCPA contributors, but we know that water vapor seeing,[16] and potential thermo-mechanical effects inside the METIS cryostat (despite it being very stable and gravity invariant) will also affect the performance of METIS HCI. Furthermore, as shown in Sec. 3.2, the chromatic beam wander effect is not even the main contributor to NCPA aberrations for the N-band, as water vapor seeing is expected to dominate.

The results of our study, therefore, suggest that a closed-loop correction of the NCPA aberrations is needed for METIS to reach its goal in terms of HCI performance. This is all the more important for N-band observations, where the contribution of water vapor seeing pulls the post-ADI contrast curves largely above the target performance. In Ref. 16, we show that a closed-loop correction of up to 100 Zernike modes at a loop repetition frequency of 10 Hz is desirable to mitigate the effect of water vapor seeing, especially at N band (please refer to Ref. 15 for a description of the wavefront sensing algorithm). Here, we illustrate the gain that such a closed-loop correction would enable in the case of chromatic beam wander, focusing on the L band where chromatic beam wander is the main source of variable NCPA (doing this exercise at N band would be moot without including water vapor seeing and is therefore left to future work—see Ref. 16 for preliminary results). This is done in Fig. 11, where we illustrate the effect of correcting only tip-tilt, 20 Zernike modes, or 100 Zernike modes, at a loop frequency of 10 Hz, using a simple integrator assuming two frames of delay in the loop and a gain of 0.4. This figure illustrates that SCAO-limited performance can be recovered up to a certain angular separation that depends on the number of corrected modes. This only pertains to phase aberrations, as we have no means to correct for amplitude aberrations in METIS. The latter may eventually set the limit to the achievable performance of the instrument.

## 5 Conclusion and Perspectives

In this work, we explored the impact of chromatic beam wander NCPA aberrations on the HCI modes of METIS. The AO and science common path differs slightly due to the different wavelengths, and the corresponding beams degrade differently as their wavefronts acquire slightly shifted SFE. Furthermore, the SCAO is unable to see and correct for the WFE gained by the science beam after the AO beam is split. This creates quasi-static aberrations in the order of $81 \pm 6$ $nm_{RMS}$ and $75 \pm 4$ $nm_{RMS}$ for the LM and N arms of the IMG, respectively (Fig. 6). These aberrations also shift slowly as the surfaces upstream of the derotator rotate with respect to the detector, creating variations of 35 $nm_{RMS}$ in 2 h, and causing a significant impact on the HCI modes of METIS, as explored in Sec. 3.2 and discussed in Sec. 4.

This was a relevant study for METIS, with its results strongly suggesting a need for a closed-loop correction of the NCPA aberrations to achieve its required HCI performance. MICADO and HARMONI are two other first-generation ELT instruments, which will also have HCI modes, working at shorter wavelengths. Their respective AO systems and optical trains are optimized for their respective wavelength bands, so extrapolating the results of the current study to these instruments would not be correct. Nevertheless, they could use similar techniques to evaluate their own performance, correction strategies, and mitigate risks earlier on.

MICADO is the MultiAO Imaging CAmera for Deep Observations, and will work on a wavelength range of 800 to 2400 nm. It will rely on a SCAO system for its standalone phase, and on Multiconjugate adaptive Optics Relay For ELT Observations (MORFEO) at a later phase.[32] It will use classical Lyot coronagraphs in the focal plane, Lyot stops, sparse aperture masking stops, and apodizing pupil masks in the pupil plane, with contrast being improved by ADI algorithms.[33] With no other special optical correction for NCPA, MICADO would benefit from running a study similar to the one presented here, to better understand its limitations and potentially develop appropriate compensation techniques.

The High Angular Resolution Monolithic Optical and Near-infrared Integral field spectrograph (HARMONI) has a very similar wavelength range (460 to 2450 nm[34]), and it relies on high-contrast AO modes with pupil plane apodizers and focal plane masks.[34] However, it contains an image slicer on their near-IR Integral Field Spectrograph (IFS) module, which makes using conventional NCPA calibration techniques problematic.[35] HARMONI is trying to use machine learning techniques to distinguish NCPA speckles from PSF aberration features. HARMONI also uses a Zernike sensor for Extremely Low-level Differential Aberrations (ZELDA) wavefront sensor operating at a wavelength of $1.175 \pm 0.050$ $\mu$m between the SCAO and IFS modules. These two modules are working at a wavelength of 0.8 $\mu$m and in a band between 1.2 and 2.4 $\mu$m, respectively. The objective is to identify and attenuate quasi-static NCPA aberrations caused by the difference between the sensing and observing wavelengths. However, chromatic beam wander is considered only as a source of sensor noise for the ZELDA sensor.[35,36] A better understanding of these NCPA effects with end-to-end simulations is essential to better train the machine learning algorithms, understand better the limitations of the ZELDA sensor, and allow a more successful calibration.

Future second-generation ELT instruments (such as ANDES, MOSAIC, and eventually PCS) would also gain from similar studies in order to mitigate problems early on. But similar studies are not limited to the European ELT, and they would also be possible to execute for the instruments of other extremely large telescopes, such as the TMT or the GMT. With the growth of telescope sizes comes the need for ever more precise instruments, with less budget for speckle noise. Understanding their nature and behavior of quasi-static speckles will help define new techniques, or optimize old techniques to avoid or calibrate them.

## Disclosures

The authors have no relevant financial interests in the current manuscript and no other potential conflicts of interest to disclose.

## Code and Data Availability

All data used and code developed for this work are specific for the case of METIS, and the authors are happy to share it within the METIS consortium. The authors do not have permission to share some of the data outside the consortium, though. Nevertheless, the authors believe that the methods here employed and described can prove helpful for other instruments.

## Acknowledgments

The authors would like to thank the whole METIS team, especially Paulo Garcia and Tibor Agócs, who guided and started this work. This project has received funding from the European Research Council (ERC) under the European Union's Horizon 2020 research and innovation programme (Grant No. 819155).

## References

1. S. Ramsay et al., "Instrumentation for ESO's extremely large telescope," *The Messenger* **182**, 3–6 (2021).
2. B. R. Brandl et al., "Status update on the development of METIS, the mid-infrared ELT imager and spectrograph," *Proc. SPIE* **12184**, 1218421 (2022).
3. R. Bowens et al., "Exoplanets with ELT-METIS. I. Estimating the direct imaging exoplanet yield around stars within 6.5 parsecs," *Astron. Astrophys.* **653**, A8 (2021).
4. B. Carlomagno et al., "METIS high-contrast imaging: design and expected performance," *J. Astron. Telesc. Instrum. Syst.* **6**, 035005 (2020).
5. C. Delacroix et al., "The High-contrast End-to-End Performance Simulator (HEEPS): influence of ELT/METIS instrumental effects," *Proc. SPIE* **12187**, 121870F (2022).
6. S. Hippler et al., "Single conjugate adaptive optics for the ELT instrument METIS," *Exp. Astron.* **47**, 65–105 (2019).
7. M. Feldt et al., "High strehl and high contrast for the ELT instrument METIS: Final design, implementation, and predicted performance of the single-conjugate adaptive optics system," *Exp. Astron.* **58**, 20 (2024).
8. R. Galicher and J. Mazoyer, "Imaging exoplanets with coronagraphic instruments," arXiv:2302.10833 (2023).
9. C. Marois et al., "Angular differential imaging: a powerful high-contrast imaging technique," *Astrophys. J.* **641**, 556–564 (2006).
10. F. Cantalloube et al., "Peering through SPHERE images: a glance at contrast limitations," *The Messenger* **176**, 25–31 (2019).
11. N. Jovanovic et al., "Review of high-contrast imaging systems for current and future ground-based and space-based telescopes: Part II. Common path wavefront sensing/control and coherent differential imaging," *Proc. SPIE* **10703**, 107031U (2018).
12. E. Huby et al., "Post-coronagraphic tip-tilt sensing for vortex phase masks: the QACITS technique," *Astron. Astrophys.* **584**, A74 (2015).
13. F. Martinache, "The asymmetric pupil Fourier wavefront sensor," *Publ. Astron. Soc. Pac.* **125**, 422 (2013).
14. S. P. Bos et al., "Focal-plane wavefront sensing with the vector-Apodizing Phase Plate," *Astron. Astrophys.* **632**, A48 (2019).
15. G. Orban de Xivry et al., "ALF: an asymmetric Lyot wavefront sensor for the ELT/METIS vortex coronagraph," *Proc. SPIE* **13097**, 130973Z (2024).
16. O. Absil et al., "Impact of water vapor seeing on mid-infrared high-contrast imaging at ELT scale," *Proc. SPIE* **12185**, 1218511 (2022).
17. M. A. Kenworthy et al., "A review of high contrast imaging modes for METIS," *Proc. SPIE* **10702**, 10702A3 (2018).
18. O. Absil et al., "METIS high-contrast imaging: from final design to manufacturing and testing," *Proc. SPIE* **13096**, 1309652 (2024).
19. D. Mawet et al., "Fundamental limitations of high contrast imaging set by small sample statistics," *Astrophys. J.* **792**, 97 (2014).
20. T. Agócs et al., "Preliminary optical design for the common fore optics of METIS," *Proc. SPIE* **9908**, 99089Q (2016).
21. T. Agócs et al., "End to end optical design and wavefront error simulation of METIS," *Proc. SPIE* **10702**, 107029O (2018).
22. S. E. Urban and P. K. Seidelmann, *Explanatory Supplement to the Astronomical Almanac*, ch. "Refraction - Numerical Integration," Section 3.281, pp. 141–143, University Science Books, Mill Valley (1992).
23. C. Y. Hohenkerk and A. T. Sinclair, "The computation of angular atmospheric refraction at large zenith angles," tech. rep., Royal Greenwich Observatory Science and Engineering Research Council (1985).
24. C. Schmid et al., "ESO-254547 – common requirements for E-ELT instruments," ESO internal document (2015).
25. J. E. Krist, "PROPER: an optical propagation library for IDL," *Proc. SPIE* **6675**, 66750P (2007).
26. G. N. Lawrence, "Optical modeling," *Appl. Opt. Opt. Eng.* **11**, 125 (1992).
27. A. Boné et al., "The Talbot effect's impact on the high contrast imaging modes of METIS," *Proc. SPIE* **11451**, 114514D (2020).

28. M. Lewińska-Maresca et al., "Development and verification of the largest cryogenic mid IR aluminium concave mirror for METIS showing excellent wavefront performance," *Proc. SPIE* **12188**, 121881P (2022).
29. D. Zaalberg et al., "Development of an aluminium mirror with a novel integrated flexure-based mount for METIS cryogenic environment," *Proc. SPIE* **12188**, 121881O (2022).
30. H. Talbot, "LXXVI. Facts relating to optical science. No. IV," *Lond. Edinburgh, Dublin Philos. Mag. J. Sci.* **9**(56), 401–407 (1836).
31. D. Gratadour et al., "COMPASS: an efficient, scalable and versatile numerical platform for the development of ELT AO systems," *Proc SPIE* **9148**, 91486O (2014).
32. A. Boné et al., "The MICADO first light imager for the ELT: a comprehensive tolerance analysis for the relay optics," *Proc. SPIE* **12184**, 1218435 (2022).
33. F. Biondi et al., "Verification strategy for the MICADO cold optics," *Proc. SPIE* **12188**, 121883P (2022).
34. N. A. Thatte et al., "HARMONI: first light spectroscopy for the ELT: instrument final design and quantitative performance predictions," *Proc. SPIE* **11447**, 114471W (2020).
35. Á. Menduiña-Fernández, M. Tecza, and N. Thatte, "HARMONI: first light spectroscopy for the ELT: novel techniques for the calibration of non-common path aberrations," *Proc. SPIE* **11447**, 114472L (2020).
36. A. Hours et al., "HARMONI at ELT: a Zernike wavefront sensor for the high-contrast module: testbed results with realistic observation conditions," *Proc. SPIE* **12185**, 121852E (2022).

Biographies of the authors are not available.